PROCEEDINGS OF THE 15TH SYMPOSIUM ON THE GEOLOGY OF THE BAHAMAS AND OTHER CARBONATE REGIONS

Edited by
Douglas W. Gamble and Pascal Kindler

Gerace Research Center
San Salvador, Bahamas
2012

Front Cover: *Porites* colony encrusted by red algae in waters of San Salvador, Bahamas; see paper by Fowler and Griffing., p. 41. Photograph by Pascal Kindler, 2011.

Back Cover:. Dr. Jörn Geister, Naturhistorisches Museum Bern, Keynote Speaker for the 15th Symposium and author of "Keynote Address – Time-Traveling in a Caribbean Coral Reef (San Andres Island, Western Caribbean, Colombia)", this volume , p. vii. Photograph by Joan Mylroie.

Press: A & A Printing

ISBN 978-0-935909-93-7

EVALUATION OF FRESH-WATER RESOURCES AT THE LINE HOLE WELL FIELD USING ELECTRICAL RESISTIVITY TOMOGRAPHY

Scot A. Russell Jr., Lee J. Florea, and Chasity L. Stinson
Department of Geography and Geology
Western Kentucky University
Bowling Green, KY 42101

ABSTRACT

A major economic constraint in the Bahamas, and other small carbonate islands world-wide, is the lack of fresh-water resources. To better address socio-economic problems on San Salvador Island, the Bahamas, we sought to gain a more detailed understanding of the extent, behavior, and controls on the island's fresh-water lens using DC electrical resistivity tomography and time-series geochemical data from the Line Hole well field, an inactive source water supply last used in December of 2006. Electrical resistivity profiles were used to image the extent and geologic framework of the fresh-water lens in this coastal setting. Time-series geochemical data provide information on the short-term behavior of fresh water in the shallow subsurface.

Inversion models of the electrical resistivity profiles illustrate a fresh-water lens that averages 3 m thick or less. However, the error statistics calculated for the electrical resistivity models indicates that there is room to improve the accuracy of the experiment. The mixing zone between fresh water and saline water is diffuse, and substantially thicker than the fresh-water lens. Geochemical results support the dimensions of the fresh-water lens predicted by the electrical resistivity model. Mixed semi-diurnal and spring/neap tidal cycles are the primary control on the water level during our period of record in the dry season; an analysis of precipitation with respect to water level and geochemistry indicate low effective recharge rates during the study period. Statistical analyses of specific conductance and temperature illustrate a positive and negative correlation with water level, respectively. Specific conductance increases with respect to depth (1,064 µS/cm to 10,881 µS/cm), and conversely temperature decreases with respect to depth (26.4 °C to 26.8 °C).

INTRODUCTION

San Salvador Island is a small "out island" or "family island", defined as an island with a small rural population in the nation's periphery outside of Nassau (Sealey, 1994). The development of the Club Med resort in 1992 (Gamble et al., 2000), supported by the Bahamian government as a means of increasing the economic well being of the residents of San Salvador, has increased the rate of fresh-water withdrawal from the Cockburn Town aquifer (Erdman et al., 1997).

These resultant water-resource problems have two major effects on the island's infrastructure. The first of these problems is addressed by Cant (1996), who reported that one of the major obstacles of economic development in the Bahamas and other small carbonate islands is limited fresh-water supplies. Second, the quality of life on the island is a function of the availability of fresh water. The increase in mean salinity in the water supply may have detrimental health effects on the local population such as sodium hypertension (Erdman et al., 1997).

To aid in our understanding of these socio-economic problems we sought a more detailed understanding of the extent, behavior, and controls on the fresh-water lens of San Salvador Island. This hydrogeological case

study of the Line Hole well field uses a combination of geochemical and geophysical techniques to study fresh-water resources in this dynamic aquifer. Results of this experiment demonstrate that the fresh-water lens on San Salvador Island can be modeled using electrical resistivity tomography (ERT), and that the fresh-water lens at the Line Hole well field is in a state of pumping-induced disequilibrium.

San Salvador Island has a rate of evapotranspiration ranging from 1,250 to 1,375 mm/yr (Sealey, 1994), and precipitation rates ranging from 500 to 2,000 mm/yr. With no surface-water component, the mean annual water budget for the island is solely dependent on this balance between precipitation and evapotranspiration (Crump and Gamble, 2006). Negative water budgets in conjunction with the presence of interdune depressions create hypersaline lakes (Figure 1). These hypersaline lakes create a cone of depression in the potentiometric surface and a contemporaneous upconing of isohaline lines that divide the fresh ground water into small, isolated fresh-water lenses under the dune ridges (Roebuck et al., 2004; Figure 1). Pumping of water wells also creates a cone of depression, which, along with upconing of isohaline lines, can also cause fragmentation of the fresh-water lens. Results by Schneider and Kruse (2005) confirm that, when anthropogenic influences are included in the water budget, the fresh-water lens is easily depleted. In the case of San Salvador Island, significant increases in pumping rates, and salinity of the water wells have been positively correlated to increases in the island's water usage due to the opening of Club Med (Erdman et al., 1997).

Using geological characteristics of islands, Whitaker and Smart (2004) have identified two carbonate aquifers, with very different permeability characteristics, that are used for water supply in the Bahamas and the Turks and Caicos Islands. The first aquifer consists of local strand-plain and beach sands from the unconsolidated to partially consolidated Holocene aquifer of the Rice Bay Formation (San Salvador Island), which is characterized by

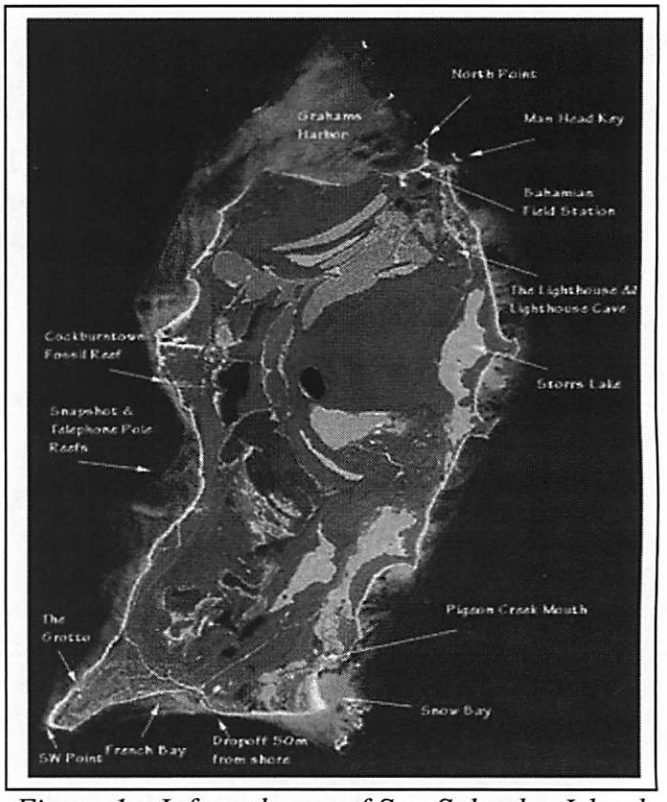

Figure 1: Infrared map of San Salvador Island adapted from Dr. Kari Benson's website: http://benson-k.web.lynchburg.edu/bahamas/sansal.html.

high primary porosity and relatively low hydraulic conductivity (Whitaker and Smart, 2004). Conversely, the principal aquifer on most islands is the Pleistocene Lucayan Limestone, which includes the Owl's Hole and Grotto Beach Formations (San Salvador Island), which has lower relative porosity, but higher relative hydraulic conductivities due to the development of dissolutionally enhanced permeability (Vacher, 1988; Whitaker and Smart, 2004). Dupuit-Ghyben-Herzberg analyses by Vacher (1988) also suggest that the fresh-water lens will be thicker in the Holocene Rice Bay Formation where permeability is lower.

The Line Hole well field includes 12 water wells used by the United Estates settlement, on the north-central shore of the island, from the mid 1990s to December, 2006. Termination of pumping in this well field was directly related to pumping-induced salt-water

intrusion. Gaughan and Davis (2009) have documented that the salinity in the wells have decreased since the pumping was terminated.

The history of the Line Hole well field provides a case example for studying the occurrence of fresh water in an area that has experienced salt-water intrusion. Gaughan and Davis (2009) cite shorter than expected tidal lag times in the well field to support the presence of phreatic conduits below the well field. This theory is also supported by large dissolutional features (banana holes) near one of the wells and elsewhere surrounding the well field (Harris, 1996). Although these banana holes cannot be directly used as evidence of conduit flow, they do illustrate the presence of dissolution voids near the well field.

METHODOLOGY

Time-series data of geochemical parameters and water-level were collected in the north abandoned well at the Line Hole well field on San Salvador Island, Bahamas (Figure 2). Two YSI multi-parameter geochemical datasondes were programmed to collect measurements from January 3, 2009 to February 19, 2009 at ten minute intervals. The following geochemical parameters were measured by the datasondes: pH, specific conductance (SpC), dissolved oxygen (DO), and temperature (T). The datasondes were installed at 7 m, and 11 m below the top of the casing for the north abandoned water well (Figure 2). Water level data was collected using two CS pressure transducers connected to Campbell Scientific CR10X data loggers, and one YSI LevelScout transducer from January 3, 2009 to June 29, 2009. The two CS pressure transducers were installed in the North 1 and southeast abandoned wells at a depth of 5 m below the top of the well casing, and the YSI pressure transducer was installed in the north abandoned water well at a depth of 10 m below the top of the well casing (Figure 2). A HOBO Onset rainfall gauge was installed at the pumping station in the center of the well field. The period of data collection for the rainfall gauge is identical to the pressure transducers. The time-series data collected from the Line Hole well field were analyzed statistically using MATLAB, and Microsoft Excel. Scatter plots, and correlograms of the time-series data were created to identify trends in the data.

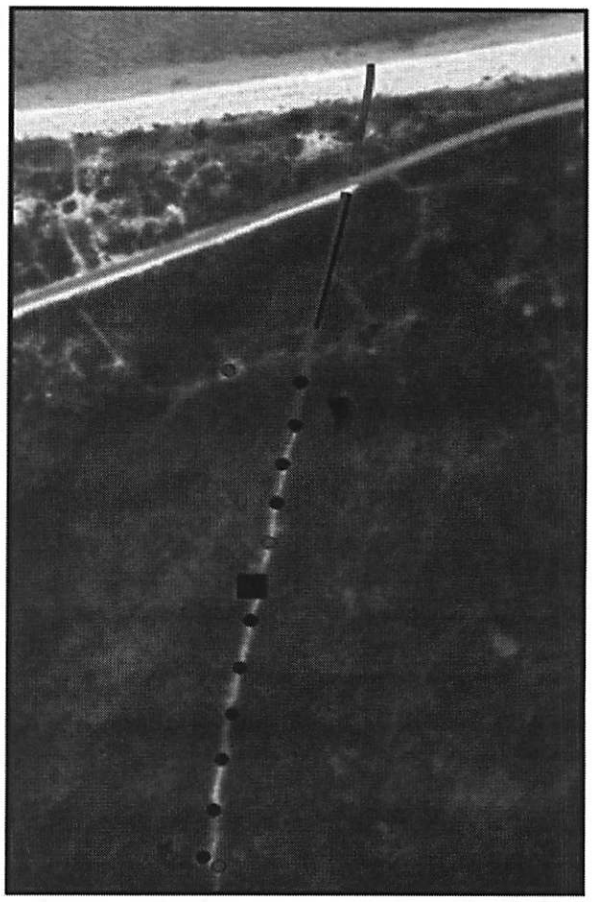

Figure 2. Diagrammatic map of the Line Hole well field with the location of data collection sites illustrated. The short line is the beach electrical resistivity transect, and the long line is the long electrical resistivity transect. The short line overlying the Long transect is the ridge electrical resistivity transect. The black circles are, from north to south, the N5, N4, N3, N2, S1, S2, S3, S4, S5, and SWA water wells. The light-grey circles are, from north to south, the NA, N1, and SEA water wells. The light-grey circles indicate data collection wells. The black square in the middle of the well field is the pump house.

DC Electrical Resistivity Tomography (ERT) transects were collected between June 29

and July 2, 2009 using an AGI Sting R1 Earth Resistivity Meter. Inversion models of the raw data were created using the AGI Earth Imager 2D software package. Three dipole-dipole arrays were utilized with electrode spacings of 2.8 m, 2.8 m, and 6.27 m, respectively (Figure 2). The first transect begins at the high-tide line (W74.4866°, N24.1164°) and extends 75.6 m inland to the north edge of the road (W74.4870°, N24.1158°). The second transect begins at the south edge of the road (W74.4861°, N24.1184°) and extends 75.6 m across the Pleistocene dune-ridge (W74.4899°, N24.1148°). The third transect begins at the south edge of the road (W74.4861°, N24.1184°) and extends 168 m inland across the Pleistocene dune ridge (W74.4889°, N24.1130°).

Using Earth Imager 2D, the following three cross-sections were generated for each ERT transect: measured apparent resistivity pseudo-section, inverted resistivity section, and calculated apparent resistivity pseudo-section. The measured apparent resistivity pseudo-section is a display of the field measurements of apparent resistivity. The inverted resistivity section is the model of the subsurface resistivity distribution based upon the measured apparent resistivities. The calculated apparent resistivity pseudo-section is a calculation of the apparent resistivity measurements based upon the predicted resistivity distribution. This last cross-section is used as a visual measure of the accuracy of the model.

RESULTS

Geochemical

The graph of water level and precipitation with respect to time (Figure 3) reveals no correlation between water level and rainfall events. Autocorrelation plots confirm the absence of a correlation between water level and precipitation due to the lack of any autocorrelation maxima corresponding to the timing of precipitation events (Figure 4). In addition, the autocorrelograms for both pH and dissolved oxygen reveal no meaningful

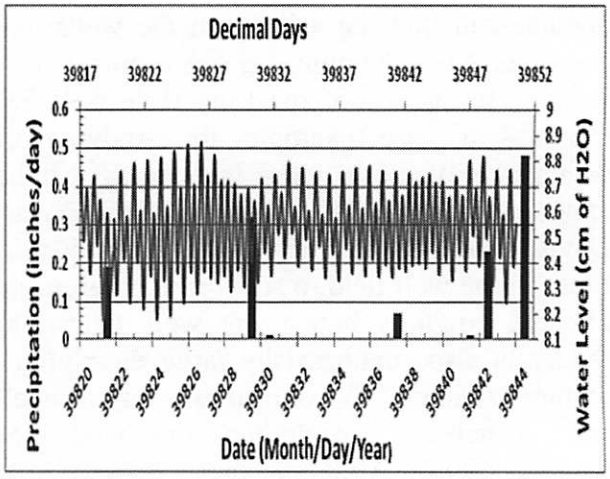

Figure 3. Time-series graph of precipitation and water level with respect to time. On the primary y-axis is precipitation (black) measured in inches per day, and on the primary x-axis is the date of rainfall events. On the secondary y-axis is water level measured at a depth of 10 m, and on the secondary x-axis is time measured in decimal days.

correlations. Conversely, two significant temporal trends are observed in the graph of water level with respect to time (Figure 3). The first trend is a mixed semi-diurnal cycle with the autocorrelation maxima occurring in the morning. The autocorrelation function of water level at 100 lags (Figure 5) confirms this mixed semi-diurnal trend. The maximum positive autocorrelation occurs at 0 lags and the maximum negative autocorrelation occurs at approximately 26 lags (4.33 hours). The second trend is also cyclic, but has a wavelength of approximately 20 days. The autocorrelation function of water level at 4,000 lags (Figure 6) confirms this trend. The primary maximum positive autocorrelation occurs at 0 lags, and the secondary maximum positive autocorrelation occurs at approximately 2,100 lags (14.58 days).

The graph of specific conductance with respect to time (Figure 7) illustrates a mixed semi-diurnal signal at both 7 and 11 m depth. With respect to depth, average specific conductance increases from 1,064 µS/cm at 7 m to 10,881 µS/cm at 11 m (Figure 7). There is a lag of approximately 0.33 hours in between the

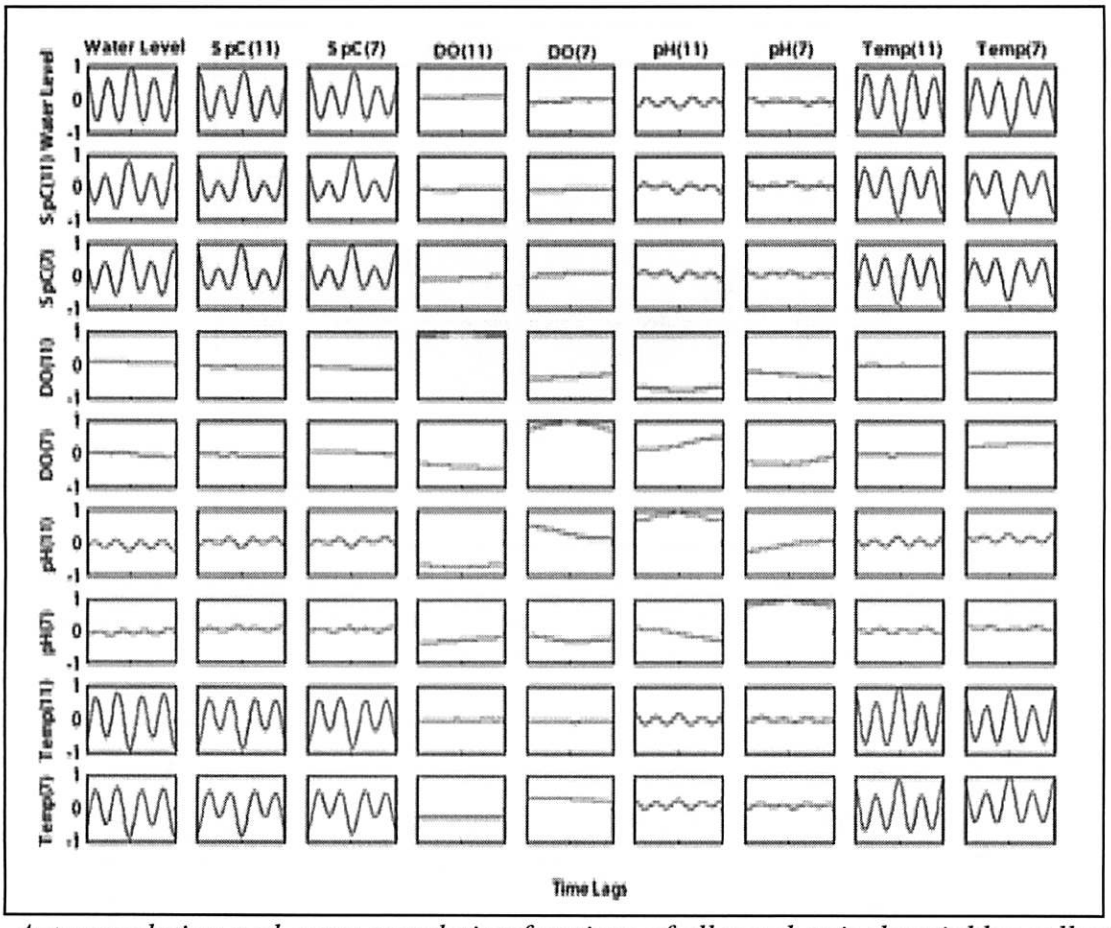

Figure 4. Autocorrelation and cross-correlation functions of all geochemical variables collected at the Line Hole well field (water level at 10 m, specific conductance at 11 and 7 m, pH at 11 and 7 m, dissolved oxygen at 11 and 7 m, and temperature at 11 and 7 m) plotted as a function of time lags. Time lags (1 lag corresponds to a 10-minute shift in time) are plotted on the x-axes of all sub-plots, and the correlation coefficient from -1 (negative correlation) to 1 (positive correlation) is plotted on the y-axes of all sub-plots.

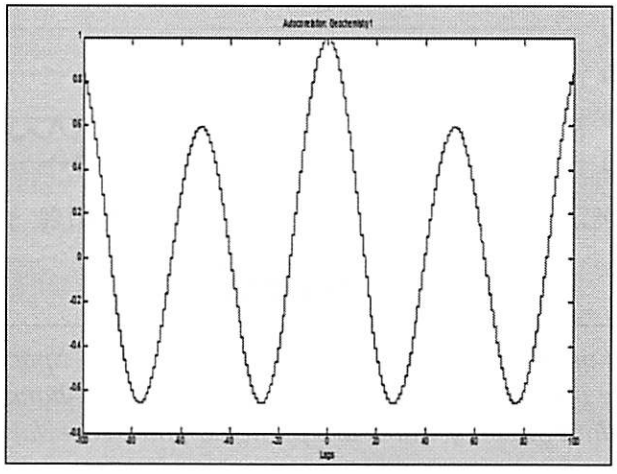

Figure 5. Graph of the autocorrelation function of dissolved oxygen data collected at 11 m depth in the North Abandoned Well with 4000 lags. On the x-axis is time in terms of lags (1 lag is equivalent to 10 minutes), and on the y-axis is the degree of autocorrelation.

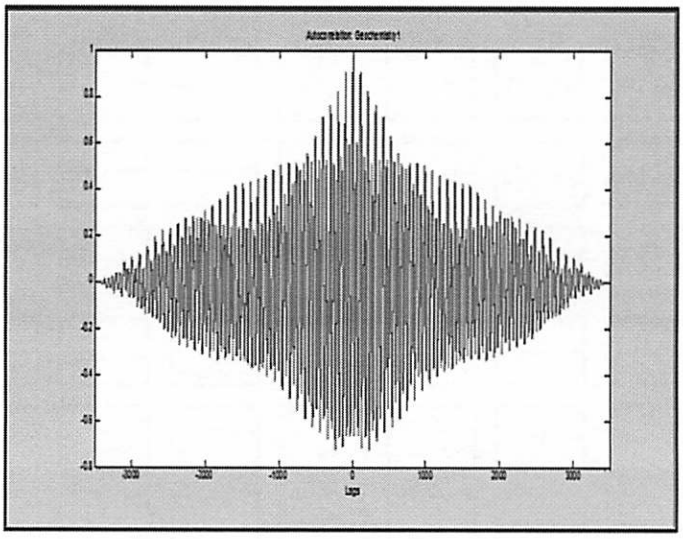

Figure 6. Graph of the autocorrelation function of specific conductance data collected at 11 m depth in the North Abandoned Well with 4000 lags. On the x-axis is time in terms of lags (1 lag is equivalent to 10 minutes), and on the y-axis is the degree of autocorrelation.

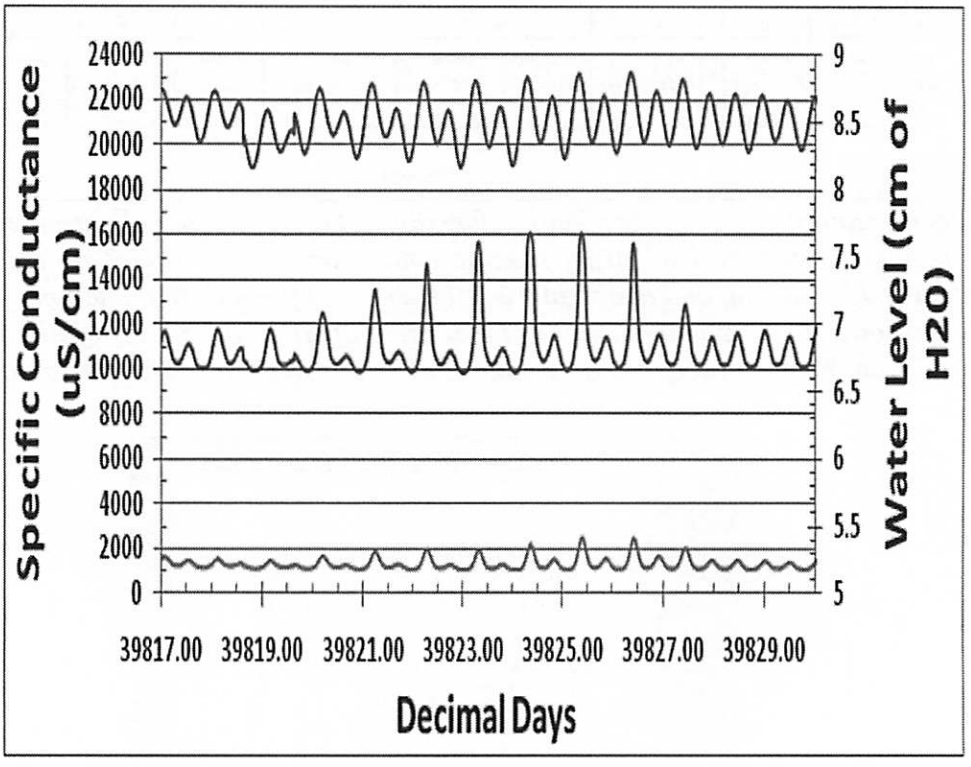

Figure 7. Time-series plot of specific conductance and water level. Specific conductance in µS/cm, at depths of 7 m and 11 m, are plotted on the primary vertical axis (left-hand axis) with respect to time in decimal days. Water level data in cm of water are plotted on the secondary vertical axis (right-hand axis) with respect to time.

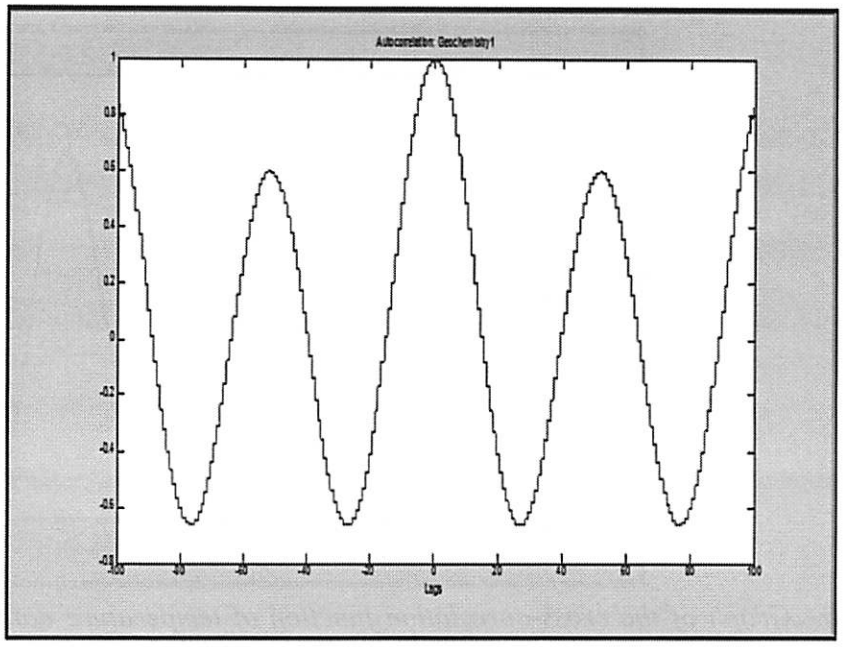

Figure 8. Graph of the cross-correlation function of specific conductance data collected at 11 m depth with respect to water level in the North Abandoned Well with 100 lags. On the x-axis is time in terms of lags (1 lag is equivalent to 10 minutes), and on the y-axis is the degree of cross-correlation.

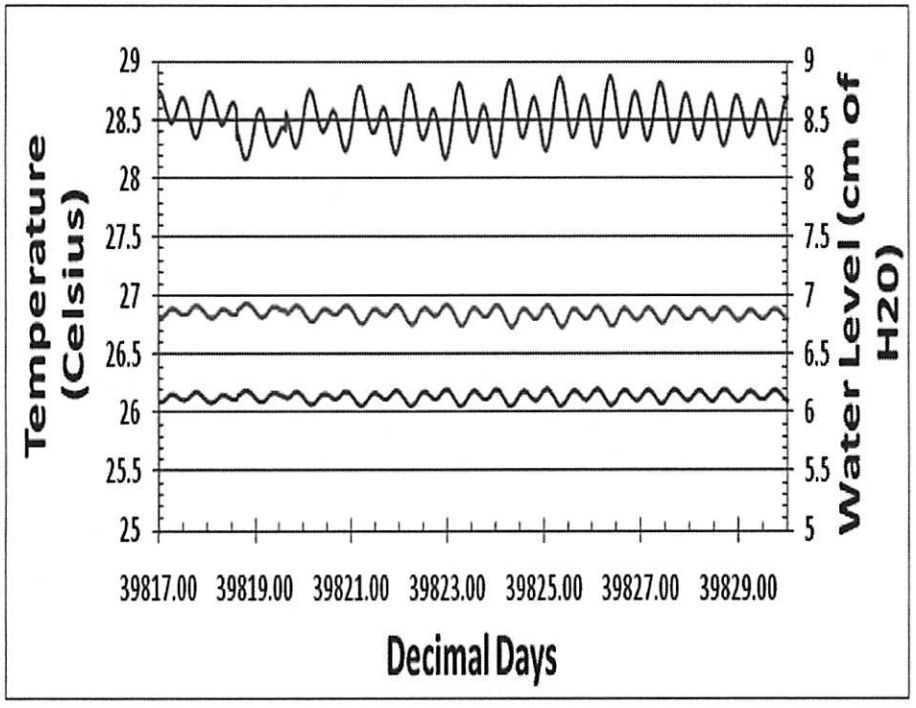

Figure 9. Time-series plot of temperature and water level. Temperature at depths of 7 m and 11 m are plotted on the primary vertical axis (left) with respect to time in decimal days. Water level data in cm of water are plotted on the secondary vertical axis (right) with respect to time.

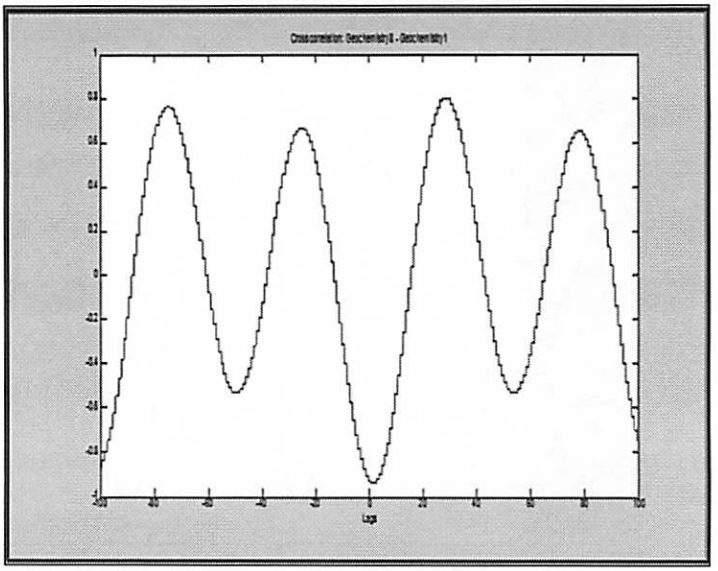

Figure 10. Graph of the cross-correlation function of temperature data collected at 11 m depth with respect to water level in the North Abandoned Well with 100 lags. On the x-axis is time in terms of lags (1 lag is equivalent to 10 minutes), and on the y-axis is the degree of cross-correlation.

water level maxima, and the specific conductance maxima. The cross-correlation function of specific conductance with respect to water level at 100 lags is used to confirm this trend and to quantify the lag (Figure 8). The maximum positive correlation between specific conductance and water level occurs at 8 lags (0.33 hours) and reaches maximum negative correlation at approximately 35 lags (4.83 hours).

The graph of temperature with respect to time (Figure 9) illustrates a mixed semi-diurnal signal at both 7 and 11 m depths. Conversely, the temporal trend in temperature is negatively-correlated with water level. With respect to depth, average temperature increases from 26.4 °C at 7 m to 26.8 °C at 11 m (Figure 9). There is a small amount of lag time in between the water level maxima, and the temperature maxima. The cross-correlation function of temperature with respect to water level at 100 lags is used to quantify this lag (Figure 10). The maximum positive correlation between temperature and water level occurs at 3 lags (0.50 hours) and reaches maximum negative correlation at approximately 30 lags (5.00 hours).

DC Electrical Resistivity Tomography

The subsurface cross section of the measured apparent resistivity at the beach transect is stratified to a depth of analysis of approximately 6.0 m with zones of high resistivity (ρ_{app}>2000 Ω·m) at 0 > z > -2.0 m, followed by a zone of medium resistivity (ρ_{app} ~ 100 Ω·m) less than a meter thick, and a zone of lower resistivity (ρ_{app} ~ 10Ω·m) at -2.0 > z > -6.0 m. Below -6.0 m the apparent resistivity distribution is mottled with resistivities ranging from approximately 50 to 0.04 Ω·m. The inversion model of the electrical resistivity for the Beach transect (Figure 11) has electrical resistivity values ranging from 1.0 to 1634 Ω·m, and has a maximum depth of penetration of 6.8 m below sea level. The model illustrates two separate zones of electrical resistivity with a transitional zone in between. Below a depth of 2 m resistivity values do not exceed 6.4 Ω·m, and above 2 m resistivity values range from 40.4 to 1634 Ω·m. This stratification is a relatively continuous feature that occurs from the swash zone at the beach across the Holocene strandplain. The model used 4 iterations, has an RMS of 65.14%, and a L2 of 412.25.

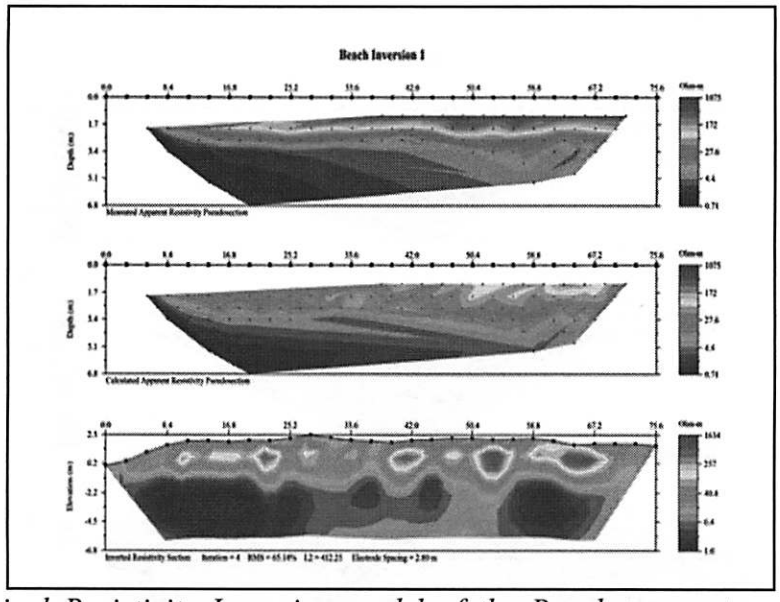

Figure 11: Electrical Resistivity Inversion model of the Beach transect generated using the Earth Imager 2D inversion software by Advanced Geosciences Inc. The Beach transect consists of 28 electrodes spaced 2.80 m, and ends at the north edge of the road. The figure consists of three cross-sections: the first is a measured apparent resistivity pseudosection, the second is a calculated apparent resistivity pseudosection, and an inverted resistivity section. Electrical Resistivity in the 75.6 m long model ranges from 1.0 to 1634 Ω·m, and has a maximum depth of penetration of 6.8 m below sea level.

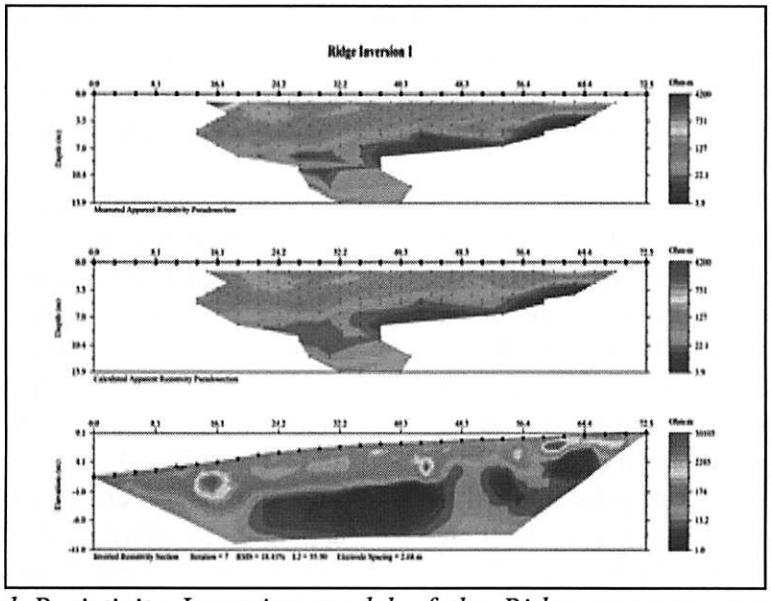

Figure 12. Electrical Resistivity Inversion model of the Ridge transect generated using the Earth Imager 2D inversion software by Advanced Geosciences Inc. The Ridge transect consists of 28 electrodes spaced 2.8 m, begins at the south edge of the road and extends up the Pleistocene ridge to about 5 m north of the North 2 water well. The figure consists of three cross-sections: pseudosection the first is a measured apparent resistivity, the second is a calculated apparent resistivity pseudosection, and the third an inverted resistivity section. Electrical resistivity in the 75.6 m Long model ranges from 1 to 30,103 Ω·m, and has a maximum depth of penetration of 11m below sea level.

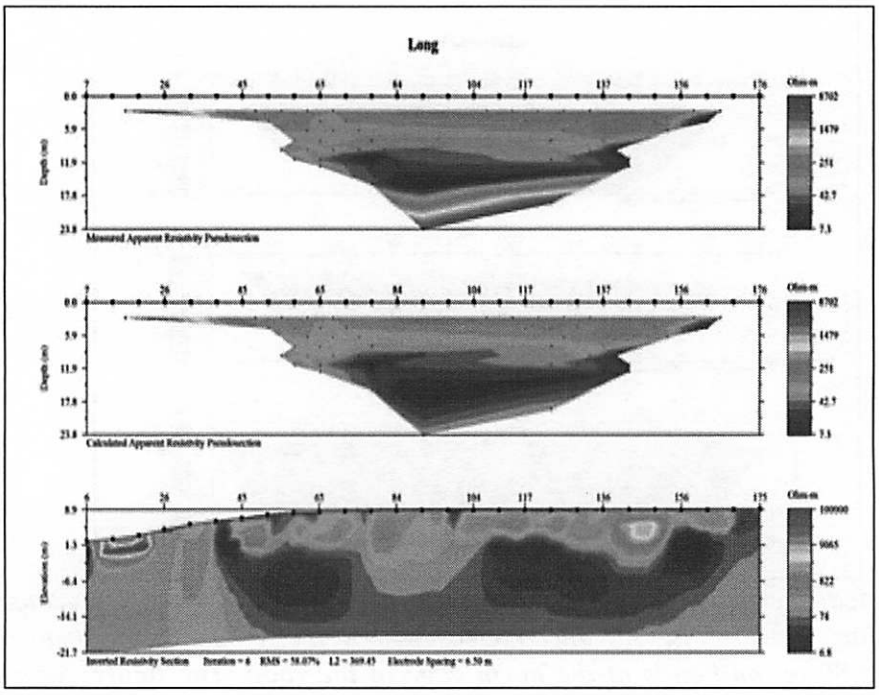

Figure 13. Electrical Resistivity Inversion model of the Long transect generated using the Earth Imager 2D inversion software by Advanced Geosciences Inc. The Long transect consists of 28 electrodes spaced 6.27 m apart, begins at the south edge of the road and extends up the Pleistocene ridge to about 5 m north of the North 2 water well. The figure consists of three cross-sections: the first is a measured apparent resistivity pseudosection, the second is a calculated apparent resistivity pseudosection, and the third an inverted resistivity section. Electrical resistivity in the 168 m Long model ranges from 6.0 to 64,404 Ω·m, and has a maximum depth of penetration of 18.0 m below sea level.

The subsurface cross section of the measured apparent resistivity at the Ridge transect is stratified to a depth of approximately 6.0 m with zones of resistivity on the order of 100 Ω·m that begin to pinch out at 30 m horizontal distance. Below 6.0 m, the apparent resistivity distribution is mottled with resistivities ranging from approximately 338 to 0.24 Ω·m. There is a large triangular anomaly, with ρ_{app}> 100,000 Ω·m, from 0.0 to 18.0 m horizontal distance that extends to a depth of approximately 5.0 m. The inversion model of the electrical resistivity for the Ridge transect (Figure 12) has electrical resistivity values ranging from 1.0 to 30,103 Ω·m, and has a maximum depth of penetration of 6.8 m below sea level. The model illustrates two separate zones of electrical resistivity, and a transitional zone similar to the inversion model of the beach. Conversely, the upper-zone of high resistivity, which ranges from approximately 100 to 30,103 Ω·m, is not laterally continuous like the Beach Inversion Model. The maximum depth of this high resistivity zone is approximately 6 m below sea level and the minimum depth is 5 m above sea level. The model used 7 iterations, has an RMS of 18.41%, and a L2 of 35.90.

The subsurface cross section of the measured apparent resistivity at the ridge transect is mottled throughout with a resistivity range of 0.08 <ρ_{app}< 10,000 Ω·m. There is a large triangular anomaly, with ρ_{app} > 100,000 Ω·m, from 0.0 to 40.0 m horizontal distance that extends to a depth of approximately 12.0 m. The inversion model of the electrical resistivity for the Long transect (Figure 13) has electrical resistivity values ranging from 6.0 to 64,404 Ω·m, and has a maximum depth of penetration of 18.0 m below sea level. The Long model

illustrates a irregular layering that mimics the Beach and Ridge models. Under most circumstances the high resistivity zone, which ranges from 65 to 64,404 Ω·m, extends to depths similar to the Ridge model. The major difference in this model is the anomalously high resistivity zone from 0 to 25 m along the transect. The model uses six iterations, has an RMS of 34.05, and a L2 of 123.53.

Temporal Geochemical Trends in the Line Hole Well Field

The primary temporal trend in Figure 3 is a mixed semi-diurnal cycle in water level, corresponding to the tides. Conversely, spring and neap tides have much larger temporal scales than the daily tidal oscillations and therefore cannot be confirmed without a larger data set. The autocorrelation function for water level at 100 and 4,000 lags (Figures 5 and 6) indicates that every 4.5 hours (27 lags) the water level in the well responds to a shift in the tides. Statistical analyses of specific conductance (Figures 8 and 10) and temperature also indicate the same temporal trend.

The Ghyben-Herzberg Principle (Ghyben, 1888; Herzberg, 1901) describes the morphology of fresh-water lenses, and geochemical stratification of water in coastal aquifers. Time-series specific conductance data collected at depths of 7 and 11 m (Figure 8) illustrate an increase in specific conductance with depth. Russell and Kane (2005) set the following intervals for specific conductance: 0-1,300 µS/cm for fresh water, 1,301-28,800 µS/cm for brackish water, and specific conductance greater than 28,801 µS/cm is considered saline. Average specific conductance at 7 m depth is 1,064 µS/cm, and at 11 m depth is 10,881 µS/cm. Using the classification system of Russell and Kane (2005), the water at 7 m depth is considered as fresh, but is bordering on brackish. The water at 11 m depth is considered as brackish, and is approximately midway between fresh and saline. Using the measured potentiometric surface depth of approximately 3 m, the fresh-

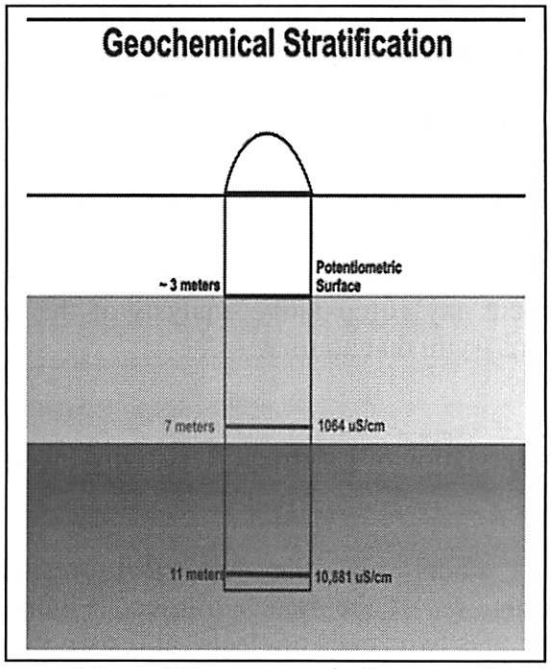

Figure 14. Diagram of the geochemical stratification in the north abandoned water well. The thresholds illustrated in the diagram are approximated according to Figure 6, and are not to scale. The potentiometric surface is at an average depth and the depth of the geochemical datasondes (7 and 11 m) is used to approximate the thickness of the potentiometric surface.

water lens is approximately 3 m thick according to the specific conductance dataset (Figure 14). The final 4 m of investigation are all in the mixing zone, and it can be assumed that the mixing zone extends several meters below the bottom of the well.

The fresh-water lens and its associated mixing zone are geochemical zones within the phreatic zone. High tide causes a rise in water level, and this process causes the fresh-water lens and mixing zone to migrate. The fixed geochemical datasondes record this movement of the fresh-water lens and provide information on its temporal behavior. Analysis of water level with respect to precipitation (Figure 3) reveals that the effects of precipitation on fresh-water lens morphology is negligible at small time scales during our period of record in the dry season. We therefore conclude that low recharge rates and tidal forcing slows the growth of the fresh-water lens and promotes the

development of a thick mixing zone. The dissolution-enhanced permeability within the Pleistocene bedrock may allows for tidal communication between the Line Hole well field and the ocean. The cross-correlogram of specific conductance with respect to water level (Figure 8) corroborate this conclusion. The lack of wells in Holocene sediment and beachrock prevent any comparative analysis of the water chemistry in that aquifer.

Interpretation of Electrical Resistivity Inversion Models

The model of the electrical resistivity distribution of the Beach transect (Figure 11) illustrates two zones of electrical resistivity with a transitional zones. This layered resistivity distribution is a relatively continuous feature that occurs from the swash zone at the beach to the end of the transect. Using common electrical resistivity values (Figure 15) there appears to be an approximately 1-m thick vadose zone with modeled resistivities over 1,000 Ω·m. The area below this 1-m thick vadose zone has a resistivity signature ranging from 100 to 1 Ω·m. This signature is indicative of various degrees of brackish water throughout the rest of the profile. The presence of the Holocene/Pleistocene lithological contact is not evident in the model, but appears in the raw apparent resistivity measurements. The lack of a lithological contact is most likely due to edge effects in the inversion models due to the position of the anomaly under the inland 6 electrodes. The Holocene dune ridge and strandplain are underlain by a thin lens of drinkable water, and a much thicker, diffuse transition zone to a depth of at least 6.8 m. These high error values indicate a high degree of noise in the data. This can be attributed to the age of the equipment used and the high conductivity of the subsurface due to saline groundwater. The relatively high porosity and permeability of the eogenetic limestones allow for large volumes of water to be held within the rock. The amount of current induced by the

Earth Resistivities for Earth Materials	
Material	**Resistivity (Ω-m)**
Igneous and Metamorphic Rocks	
Granite	$5 \cdot 10^3 - 10^6$
Basalt	$10^3 - 10^6$
Slate	$6 \cdot 10^2 - 4 \cdot 10^7$
Marble	$10^2 - 2.5 \cdot 10^8$
Quartzite	$10^2 - 2 \cdot 10^8$
Sedimentary Rocks	
Shale	$8 - 4 \cdot 10^3$
Sandstone	$20 - 2 \cdot 10^3$
Limestone	$50 - 4 \cdot 10^2$
Soils and Waters	
Clay	1 - 100
Alluvium	10-800
Fresh Groundwater	10-100
Sea Water	0.2

Figure 15. Commonly used electrical resistivity values for earth materials. This figure was adapted from a previously existing table generated by Loke (2000).

Sting R1 Earth Resistivity is not high enough to effectively resolve finer differences in the subsurface resistance due to large volumes of saline groundwater. Newer versions of this equipment induce a much larger current into the subsurface, and therefore amplify the contrast between materials.

The model of the electrical resistivity distribution of the Ridge transect (Figure 12) illustrates two zones of electrical resistivity with associated transitions, similar to the inversion model of the Beach transect. The upper zone of high resistivity ranges from approximately 100 to 30,103 Ω·m and is not laterally continuous like the inversion model of the Beach transect. The maximum depth of this high-resistivity zone is approximately 6 m below sea level and the minimum depth is 5 m above sea level. Modeled resistivity values that exceed 1,000 Ω·m are indicative of a vadose zone. Using the occurrence of these high resistivity models allows us to approximate that the vadose zone in this area varies from a depth of 2 m below the

surface at the beginning of the profile to a depth of 1 m below the surface at the top of the Pleistocene dune ridge. The thickness of this vadose zone ranges from 1 to 2 m depending on the position along the profile. The fresh-water lens is associated with resistivities ranging from 1 to 100 Ω·m. The thickest zone of fresh water occurs at approximately 16 m due to the presence of a lithological contact between Holocene and Pleistocene rocks. This feature is not illustrated in the model, but is observable in the measured pseudosection. The Holocene sands act as a hydrological barrier which causes the fresh water to accumulate along this contact in the Pleistocene aquifer (Vacher, 1988). Despite the high accuracy relative to the other profiles, the noise generated by the conductive subsurface still causes an undesirable amount of error.

The model of the electrical resistivity distribution of the Long transect (Figure 13) illustrates two zones of electrical resistivity with associated transitions, similar to the inversion model of the Beach transect. Under most circumstances, the high-resistivity zone ranges from 65 to 64,404 Ω·m, and extends to depths similar to the Ridge model. The depths of the hypothesized fresh-water lens and mixing zone in this model correspond moderately well with the geochemical data from the north abandoned water well. The basal contact of the mixing zone is not evident in the model presumably due to the lack of resolution with depth inherent in the dipole-dipole array. Along with the stratified electrical resistivity distribution, the Long model has an anomalously high resistivity zone from 0 to 25 m along the transect. This feature can either be explained by effects of the Holocene/Pleistocene lithological contact, or an error in the model.

Synthesis of Time-Series Data and Electrical Resistivity Models

Both datasets provide meaningful information on the behavior and morphology of the fresh-water lens at the Line Hole well field. The geochemical data reveal tidal influences on the fresh-water lens position, and provide a one-dimensional profile of geochemical stratification at the north abandoned water well (Figure 14). Conversely, the analysis of geochemical data is short term and only spans part of the dry season. It is therefore difficult to gain an accurate understanding of the fresh water resources on the island without a longer-term dataset. The inversion models of electrical resistivity, which image the fresh-water lens and mixing zone, lack accuracy due to the high noise levels. In terms of the accuracy of this method, the equipment being used is a large factor. Since it is often difficult to accurately delineate the potentiometric surfaces, further analyses of the models can be misleading. Despite the pitfalls, the extent of the fresh-water lens and mixing zone can be approximated using this method. When these models are cross-referenced to the geochemical analyses, there is agreement on the dimensions of the fresh-water lens on the Pleistocene dune ridge (Figures 11, 12, 13, and 14). Both datasets indicate a thin lens of fresh drinking water that is underlain by a thick, diffuse zone of mixing. Unfortunately, without wells in the Holocene strandplain, it is impossible to accurately compare geochemical data with the inversion model of the Beach transect. Despite these errors, the results gathered in this case study indicate that this method has some effectiveness in this setting.

CONCLUSIONS

Geochemical and electrical resistivity data collected at the Line Hole well field from January 1 to June 29, 2009 are used to describe the extent and behavior of fresh-water resources on San Salvador Island, the Bahamas. The following conclusions were reached using this data. (1) The north abandoned water well is likely connected through preferred flowpaths to the ocean. This connection is evident by the mixed semi-diurnal signal in the water level data with little to no lag from predicted tides. (2) The pumping, that ceased in December of 2006, has caused a depletion of the fresh-water

lens that still exists today. The thickness of the mixing zone at the north abandoned water well in the Line Hole well field exceeds 4 m, and is thicker than the fresh-water lens. (3) Noise generated from the highly conductive subsurface creates abnormally high levels of error, and makes the interpretations limited under the current conditions; updated equipment with a capacity to induce a larger current in the subsurface can limit the noise, and therefore limit the error. (4) Finally, despite the noisy electrical resistivity data, the size and extent of the fresh-water lens, and of the mixing zone underlying the Line Hole well field can be approximated.

REFERENCES

Cant, R.V., 1996, Water supply and sewage treatment in a small island environment: the Bahamian experience., *in* Maul, G.A., ed., Small islands: marine science and sustainable development, Washington D.C.: American Geophysical Union, p. 329-340.

Crump, M.A., and Gamble, D.W., 2006, Hydroclimatic analysis of a carbonate island pond through the development of a hydrologic landscape unit model: Physical Geography, v.27, p. 554-570.

Erdman, J.S., Key, Jr. M. M, and Davis, R.L., 1997, Hydrogeology of the Cockburn Town Aquifer, San Salvador Island, Bahamas, and the change in water quality resulting from the development of a resort community, *in* Curran, H.A., ed., Proceedings of the Eighth Symposium on the Geology of the Bahamas and Other Carbonate Regions: Bahamian Field Station, San Salvador, p. 47-58.

Gamble, D.W., Brown, M.E., Parnell, D., Brommer, D., and Dixon, P.G., 2000, Lessons learned from field evaluation of Hurricane Floyd damage on San Salvador Island, Bahamas: Bahamas Journal of Science, v. 8, p. 25-31.

Gaughan, M., and Davis, R.L., 2009, Water quality changes in a karst aquifer following abandonment of a well field: Line Hole, San Salvador Island, Bahamas: Geological Society of America Abstracts with Programs, v. 41, p. 466.

Ghyben, H. W., 1888, Nota in verbandmet de voorgenomen puto boring nabij Amsterdam: Tijdschrift van Let Koniklijk Instituut can Ingenieurs, The Hague, Netherlands, p. 8-22.

Harris, J. G., 1996, An Analysis of Banana Hole Development on San Salvador Island, Bahamas: Unpublished M.S. Thesis, Department of Geosciences, Mississippi State University.

Herzberg, A., 1901, Die Wasserversorgungeiniger Nordseebader: Wasserversorgung, v. 44, p. 815-819 `and 842-844

Loke, H.M., 2000, Electrical imaging surveys for environmental and engineering studies: a practical guide to 2-D and 3-D surveys, www.heritagegeophysics.com.

Roebuck, L., Pochatila, J., and Ortiz, T., 2004, Water Resource Assessment of the Bahamas: US Army Corps of Engineers, Mobile District and Topographic Engineering Center.

Russell, G.M., and Kane, R..L., 2005, Bathymetry, Freshwater Flow, and Specific Conductance of Matlacha Pass, Southwestern Florida: Water Resources Investigations Report 93-4057, U.S.

Department of the Interior, U.S. Geological Survey.

Schneider, J.A., and S.E. Kruse, 2005, Assessing natural and anthropogenic impacts on freshwater lens morphology on small barrier islands: Dog Island and St. George Island, Florida: Hydrogeology Journal, v. 14, p. 131-145.

Sealey, N., 1994, Bahamian Landscapes: An introduction to the Geography of the Bahamas (Second Edition): Media Publishing, Nassau, Bahamas.

Vacher, H.L., 1988, Dupuit-Ghyben-Herzberg analysis of strip island lenses: Geological Society of America Bulletin, v. 100, p. 580-591.

Whitaker, F.F., and Smart, P.L., 2004, Hydrogeology of the Bahamian Archipelago, *in* Vacher, H.L., and Quinn, T.M., eds, Geology and Hydrogeology of Carbonate Islands: Developments in Sedimentology, v. 54, p. 183-216.